

This article appeared in a journal published by Elsevier. The attached copy is furnished to the author for internal non-commercial research and education use, including for instruction at the authors institution and sharing with colleagues.

Other uses, including reproduction and distribution, or selling or licensing copies, or posting to personal, institutional or third party websites are prohibited.

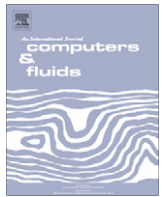
In most cases authors are permitted to post their version of the article (e.g. in Word or Tex form) to their personal website or institutional repository. Authors requiring further information regarding Elsevier's archiving and manuscript policies are encouraged to visit:

<http://www.elsevier.com/copyright>



Contents lists available at ScienceDirect

Computers & Fluids

journal homepage: www.elsevier.com/locate/complfluid

Universal instability modes in internal and external flows

Tapan K. Sengupta^{*}, V.V.S.N. Vijay, Neelu Singh

High Performance Computing Laboratory, Department of Aerospace Engineering, I.I.T. Kanpur 208 016, India

ARTICLE INFO

Article history:

Received 5 November 2009

Received in revised form 4 September 2010

Accepted 7 September 2010

Available online 16 September 2010

Keywords:

Multiple Hopf-bifurcations
 Proper orthogonal decomposition
 Landau–Stuart–Eckhaus Equation
 Anomalous modes
 Circular cylinder
 Lid-driven cavity

ABSTRACT

Two prototypical external and internal flows have been studied which display linear temporal instability followed by nonlinear saturation taking the flows to a new equilibrium state. Direct simulation results are obtained using a specific formulation and numerical methods with very high accuracy. These results are analyzed via proper orthogonal decomposition (POD), which reveal similar modes for flow past a circular cylinder and flow inside a lid-driven cavity, indicating universality of such modes. Unlike many other efforts on reduced order modeling via POD, here the emphasis has been on understanding the physical aspect of the flow instability which requires very high accuracy of the simulation. Then, the obtained POD modes are related to the instability modes (in the classical sense of defining the latter) and new generic types of instability modes are identified in the studied external and internal flows. These new modes have been reported for flow past a circular cylinder [Sengupta TK, Singh N, Suman VK. Dynamical system approach to instability of flow past a circular cylinder. *J Fluid Mech* 2010;656:82–115] which help one in understanding the instability sequence and the relative importance of these modes in the flow evolution starting from an impulsive start. Present comparative study, furthermore, reveals universality of such instability modes by showing their presence for the flow inside a lid-driven cavity as well. Despite seeming dissimilarities between these two flows, similarities between the instability portrait of these two flows suggest universality of such modes. From the equilibrium amplitude of vorticity time-series, we establish the presence of multiple modes and multiple bifurcation sequences for these flows in parameter space. Existing theory due to Landau and Stuart that considers only a single dominant mode and its self-interaction does not explain all these features. We invoke a multi-modal interaction model in the cited reference above, termed as Landau–Stuart–Eckhaus (LSE) equation in recognition of Eckhaus' work in modifying the classical Stuart–Landau equation. We also show that the new instability modes do not follow either the classical Stuart–Landau or the newly proposed LSE model equations and for this reason we call these as *anomalous modes*. Two specific classes of anomalous modes are identified and classified in the present work. Empirical expressions for the evolution of these anomalous modes are presented and their unambiguous role during instabilities is discussed.

© 2010 Elsevier Ltd. All rights reserved.

1. Introduction

There are many internal and external vortex dominated flows which display exponential temporal growth of small omni-present disturbances. Once these disturbances grow in amplitude, nonlinearity plays a decisive role in taking the system from the initial equilibrium state to another. The initial state (which could be steady or unsteady) is destabilized first and then taken to another equilibrium state. Vortex shedding behind circular cylinder is a typical example of an external flow where the steady state is destabilized temporally followed by nonlinear saturation taking the flow to the state representing the Bénard–Kármán vortex shedding. The latter equilibrium state can represent single or multiple time-periodic state. The initial instability occurs when a bifurcation parameter

is above a critical value and this passage occurs through Hopf-bifurcation(s) – as described in [40] for flow past a circular cylinder. This flow is discussed: (i) In [7], as *the local and global duality of nonparallel flow instabilities* and (ii) in [8,24,27,36,42] as a nonlinear dynamical system representing phase transition and instabilities. In the presence of nonlinearity, most of these dynamical system studies used Stuart–Landau equation [9,20,44] for the amplitude of the instability mode, as defined in [9] and explained here with the help of Eq. (6) – which is strictly valid for a system dominated by a single mode.

It has been shown in [40] and here that there are more than one dominant modes present in many of these vortex dominated flows. This has been achieved by proper orthogonal decomposition (POD) of the results of direct simulation of Navier–Stokes equation for two-dimensional flows past a circular cylinder and inside a lid-driven cavity. The original goal of POD was to project a stochastic dynamical system onto an optimal reduced order deterministic

^{*} Corresponding author. Tel.: +91 512 2597945; fax: +91 512 2597561.

E-mail address: tksen@iitk.ac.in (T.K. Sengupta).

basis model, derived using POD, which was pioneered by Kosambi [18]. Subsequent activities have gone, predominantly, along two major directions. Applying POD for fluid flow was started by Lumley and co-authors, as described in [13], with the primary intention of seeking a coherent physical picture of turbulent flows. This was facilitated by the method of snapshots, pioneered by Sirovich [41], although some alternate approaches were tried which are more computationally intensive – see e.g. [34]. In this latter reference, instead of studying turbulent flows, POD of direct simulation of bypass transition data was performed. Similarly, flow instability has been variously studied in [24,33,40] using POD by treating it as a dynamical system. However, in early applications of POD, it was performed with the assumption that the dynamical system is characterized by limit cycle oscillation, and hence the resultant spatial modes are appropriate only for the limit cycle. In order to enlarge the range of application to express the transient state as well, the authors in [24,33] used “the steady solution of the flow as an additional data point in order to achieve a model with correct transient dynamics [33].” This has been variously termed as the shift mode [24] or mean flow mode [33] and according to [33], “shift mode in essence adds one degree of freedom to the model, which enables the model to account for changes of the length of recirculation zone.” It was furthermore acknowledged that even this additional modelling efforts did not represent fluctuations and there are mismatches between the transient dynamics of the model and the Navier–Stokes solution in terms of the initial growth rates. In [24], further attempt was made to account for this shortfall by incorporating spatial modes obtained from a linear stability analysis to POD modes. While performing linear stability analysis is not always straightforward, Siegel et al. [33] concluded that “POD in its original form is not well suited to describing transient data sets.” The authors continue to state that POD modes fail to reproduce dynamic behaviour, if all available data from different flow conditions are processed *en bloc*. In calculating POD modes for a cavity flow, authors in [16] used a method called the sequential POD to process data from different flow states. This method represents dynamic behaviour better than regular POD, as the modes are ensured to be orthogonal.

In contrast to the above discussion, authors in [40] have solved Navier–Stokes equation with strict check on controlling phase and dispersion error of numerical solution and subsequently performed POD, as has been proposed in [13] and implemented by following the method of snapshot [41]. Obtained POD modes have been used to compute the corresponding instability modes (these are as given in [9,44] and different from the *stability modes* of [24]) and two new classes of modes have been reported.

The first class of modes has resemblance with the shift mode of [24,33]. Apart from the fact that this modes emerge naturally from a straightforward application of POD without requiring any modeling, there is also the essential difference that these are more than one in number. It has been clearly noted in [22] that a single shift mode is essential to a low-order minimum POD Galerkin representation of natural transients for models with flow control as the primary goal. The second class of modes in [40] show the POD amplitude function to have wave-packet like feature. These amplitude functions were obtained as an inner product of the direct simulation results with the spatial eigenmodes. This is somewhat different than that is pursued in other efforts [8,22,24,33] where dynamical model for POD amplitude functions are obtained via Galerkin projection on the Navier–Stokes equation. It has been noted in [8,24,28] that the set of equations is often structurally unstable when integrated numerically and an explanation is provided for this instability. Interestingly, the authors in [33] state that for all Galerkin models there is a need to add a linear term which requires prior calibration using experimental or computational data, which obviates the need for spatial derivatives whose

evaluation in the presence of uncertain data is the source of problem. However, our direct approach of finding the POD amplitude function removes any such problems.

We are not aware of any previous efforts where the solution of POD amplitude equations thus obtained displayed the anomalous behaviour of these two classes of modes. One reason for this could be due to the limiting assumptions employed in deriving the equations and secondly, it may be due to the stiffness of such equations due to interactions of multiple modes, as has been demonstrated in [40] via two leading mode interactions. However, here the amplitude functions are directly obtained by taking the inner product of the disturbance quantities with the spatial eigenmodes.

In many published works in recent times, emphasis has been placed on modeling the system dynamics with flow control in mind – see e.g. works reported in [22,33] and other references cited therein. These approaches of underemphasizing of transient state via the usage of a very limited number of POD modes have been justified on the ground that the “size of problem that is within reach of current control tools.” However, in the present work, our interest is more from understanding the unifying nature of accurately calculated POD and instability modes for an external and an internal flow, following the procedure of [40].

Following the above discussion, it is apparent that the accurate computation of Navier–Stokes equation is very essential in obtaining the POD eigenmodes and their time-dependent amplitude functions. If these are not obtained accurately, corresponding instability modes also would not be predicted correctly. Moreover, treating the dynamics of instability modes by Stuart–Landau equation is questionable (even if normal mode approach is invoked), because one is looking at a nonlinear system and superposition of normal modes does not hold true anymore. Stuart–Landau equation holds only when one assumes that there is only a single dominant mode and the nonlinearity is simply due to self-interaction only, as suggested in [9,20,44]. In a marked departure, the authors in [40] have replaced Stuart–Landau equation by LSE equation incorporating nonlinear multi-modal interactions by the eigenfunction expansion approach of Eckhaus [10]. They report an analysis for the flow past circular cylinder to explain multiple Hopf-bifurcations. Another achievement in [40] was to relate POD modes with instability modes using dynamical system approach [9,13]. This led to identifying the above mentioned two new classes of modes which do not satisfy either Stuart–Landau or LSE equations and hence, these modes have been termed as anomalous modes.

Bruneau and Saad [4] investigated the temporal instability of the lid-driven cavity flow and noted the critical Reynolds number (Re_{cr}) for the onset of periodicity to be in the range of $8000 \leq Re_{cr} \leq 8050$. In [30], the critical Reynolds number was extrapolated to be at $Re_{cr} = 8031.92$, while in [25], the Hopf bifurcation is noted to begin at $Re_{cr} = 7402 \pm 4$. In [11], the critical Reynolds number is found approximately equal to 8000; Poliashenko and Aidun [26] reported a value of $Re_{cr} = 7763$ while Cazemier et al. [6] reported $Re_{cr} = 7819$. The exact value for the critical Reynolds number depends upon the choice of numerical methods, the accuracy with which the boundary conditions are applied (specifically the top lid condition), and added numerical dissipation along with effectiveness of dissipation discretization playing a major role. These numerical aspects have been taken up in detail, while developing an extremely accurate combined compact scheme – NCCD scheme – in [37,38]. For the flow at $Re = 8500$ and $10,000$, multi-periodic nature of vorticity field with respect to time was noted [37,38]. It is interesting to note that the solution obtained by using NCCD scheme reported a new equilibrium solution. In this configuration, one notices a triangular vortex at the core, that is surrounded by three secondary vortices as satellites. While, triangular vortices were noted experimentally in [3,5], perhaps it was the first instance where such triangular vortices were noted

computationally in [37,38] via the solution of Navier–Stokes equation.

2. Governing equations and numerical methods

The governing two-dimensional Navier–Stokes equation for these two prototypical flows is solved in stream function–vorticity formulation [35–39] as given by,

$$\nabla^2 \psi = -\omega \quad (1)$$

$$\frac{\partial \omega}{\partial t} + \vec{V} \cdot \nabla \omega = \frac{1}{Re} \nabla^2 \omega \quad (2)$$

where ω is the only non-zero out-of-plane component of vorticity. The velocity vector is related to the stream function as $\vec{V} = \nabla \times \vec{\Psi}$, where $\vec{\Psi} = [00\psi]^T$ and Re is the Reynolds number. For the flow inside a square lid-driven cavity (LDC), the side of the square and the velocity of the lid are used as length and velocity scales, respectively, whereas for the flow past a circular cylinder, the diameter of the cylinder and the free stream velocity are used as length and velocity scales respectively, to nondimensionalize flow variables and to define flow Re . The time scale for nondimensionalization is derived from these length and velocity scales. The $(\psi - \omega)$ formulation is preferred to primitive variable formulation due to its inherent accuracy and computational efficiency in satisfying mass conservation and solenoidality everywhere for 2D flows.

For the flow in LDC [37,38], a uniform structured grid of 256 points along each of the x and y directions is used. Eqs. (1) and (2) were solved subject to the following boundary conditions to obtain the solution.

On all the four walls of LDC, $\psi = \text{constant}$ is prescribed that arises due to the no-slip and no-penetration boundary conditions; $\omega_b = -\frac{\partial^2 \psi}{\partial n^2}$ is applied on the walls to obtain the boundary vorticity (with n as the wall normal co-ordinates on individual segments of the wall) and this is calculated using Taylor's series expansion at the wall boundaries incorporating the appropriate velocity conditions at the wall. For this flow, the top lid moves horizontally with a unit nondimensional velocity, while all other walls are stationary. To solve Eq. (1), Bi-CGSTAB method, a fast and convergent elliptic PDE solver has been used here. The convection and diffusion terms were discretized using the NCCD method [37,38] that obtains both first and second derivatives simultaneously; whereas for the time derivative, four-stage, fourth-order Runge–Kutta (RK4) method is used. These methods have been rigorously analyzed for their spectral resolution and effectiveness in discretizing the dissipation terms along with the dispersion relation preservation (DRP) properties with respect to 1D-linear convection equation, before being implemented to some other flows in [37,38]. It was noted that the NCCD method serves to be very efficient and provides high resolution along with effective dissipation discretization. Additionally, it has inherent ability to control aliasing error and spurious numerical mode arising out of convection terms [38]. However, this method can be used only with uniform structured grids.

For flow past a circular cylinder, Eqs. (1) and (2) have been transformed into the (ξ, η) -plane for computational efficiency [36,39,40] and the governing equations are given by,

$$\frac{\partial}{\partial \xi} \left(\frac{h_2}{h_1} \frac{\partial \psi}{\partial \xi} \right) + \frac{\partial}{\partial \eta} \left(\frac{h_1}{h_2} \frac{\partial \psi}{\partial \eta} \right) = -h_1 h_2 \omega \quad (3)$$

$$h_1 h_2 \frac{\partial \omega}{\partial t} + h_2 u \frac{\partial \omega}{\partial \xi} + h_1 v \frac{\partial \omega}{\partial \eta} = \frac{1}{Re} \left\{ \frac{\partial}{\partial \xi} \left(\frac{h_2}{h_1} \frac{\partial \omega}{\partial \xi} \right) + \frac{\partial}{\partial \eta} \left(\frac{h_1}{h_2} \frac{\partial \omega}{\partial \eta} \right) \right\} \quad (4)$$

where h_1 and h_2 are the scale factors of transformation given by: $h_1^2 = x_\xi^2 + y_\xi^2$ and $h_2^2 = x_\eta^2 + y_\eta^2$. The subscripts indicated by Greek

alphabets indicate partial derivatives with respect to that transformed variable. This formulation satisfies divergence free or solenoidality condition for velocity and vorticity. Since pressure is eliminated while obtaining the stream function and vorticity transport equations, numerical problems arising out of pressure–velocity coupling are avoided.

However, to obtain the loads (lift and drag coefficients), a Poisson equation for the total pressure (P), is solved [39,40], which is obtained by taking the divergence of the momentum equation in rotational form and is given in transformed system as,

$$\frac{\partial}{\partial \xi} \left(\frac{h_2}{h_1} \frac{\partial P}{\partial \xi} \right) + \frac{\partial}{\partial \eta} \left(\frac{h_1}{h_2} \frac{\partial P}{\partial \eta} \right) = \frac{\partial}{\partial \xi} (h_2 v \omega) - \frac{\partial}{\partial \eta} (h_1 u \omega) \quad (5)$$

In solving the flow past circular cylinder, no-slip boundary condition is applied on the cylinder wall as,

$$\left(\frac{\partial \psi}{\partial \eta} \right)_{\text{body}} = 0$$

$$\psi = \text{constant}$$

These boundary conditions are used to solve (3) and to calculate the wall vorticity (ω_b), that in turn provides the wall boundary condition for (4). At the outer boundary for flow past a cylinder, uniform flow (Dirichlet) boundary condition is provided at the inflow, while convective (Sommerfeld) boundary condition is provided on the radial velocity at the outflow [39,40]. For Eq. (5), the boundary condition obtained from the wall-normal momentum equation is applied at the wall and at the farfield for flow past a cylinder.

The convection terms of Eq. (4) are discretized using high accuracy DRP method [38,39] for flow past a cylinder that provides near-spectral accuracy. Second order central differencing scheme is used to discretize the Laplacian operator of Eqs. (3) and (4) and the RK4 scheme is used for marching in time. A sixth-order non-periodic filter is applied on the vorticity to remove spurious disturbances due to aliasing and other nonlinear instabilities [38]. Eq. (3) is also solved using the Bi-CGSTAB method.

Both the flows are started impulsively, for the following reason in solving unsteady Navier–Stokes equation. According to Telionis [45] “many practical engineering problems can be solved approximately, by assuming that the external disturbance is impulsive ... changes of boundary conditions may therefore be considered, with a reasonable accuracy, as impulsive. This is specially true of unsteady separation.” Also, the author noted furthermore that “the early stages of impulsive viscous flows contain valuable information on flow properties that control the subsequent development of the phenomenon and a thorough understanding of its properties is essential in the study of unsteady flows.” The readers' attention is drawn to the fact that different start-ups have been studied by some authors which include the work on accelerated flow past a symmetric airfoil [35] where three prototypical start-ups including impulsive start were considered. We emphasize that impulsive start provides a consistent initial condition in studying the receptivity aspect of flow fields. This is due to the fact that impulsive start by its very nature excites widest possible bandwidth of circular frequencies and hence, would be able to latch onto the unstable frequency naturally. This is also the reason for which one undertakes study of impulse response and this is adopted for both the flows studied here.

It is to be noted that a different start-up can lead a flow to settle down to a different equilibrium solution, as has been shown in [35] for flow past an aerofoil and in [31] for flow past a circular cylinder. Sarpakaya [31] studied the effects of uniform acceleration for flow past a circular cylinder by defining a non-dimensional acceleration parameter A_p given by,

$$A_p = D \frac{dU_\infty}{dt} / \bar{U}_\infty,$$

where D is the diameter of the cylinder and \bar{U}_∞ is the final velocity and U_∞ is the instantaneous velocity. It was noted that for $A_p > 0.27$, the drag coefficient beyond the period of initial acceleration does not measurably depend upon A_p and the flow can be considered as impulsively started. Similarly, the authors in [35] noted that the effects of acceleration has most pronounced effect when the first bubble forms over the surface. Thus, the decided dependence of start-up condition is not trivial and the impulsive start is considered a standard benchmark condition and in many experimental set-ups this is usually the case, until and unless it is not practised on purpose.

It is also well known that impulsively started flows are initially inviscid. Thus, for the flow past the circular cylinder, initial condition is given by the analytically obtained inviscid solution and vorticity is generated only at the wall at $t = 0$ that is subsequently diffused and convected following the vorticity transport equation. In case of flow inside the LDC, fluid is stagnant at $t = 0$ with the lid started impulsively. This also creates wall vorticity which is transported subsequently. Thus, the initial start-up of both the flows are identical and provides a good basis for comparison.

3. Vorticity dynamics for flow past a circular cylinder and inside a square lid-driven cavity

In Fig. 1, computed vorticity values are plotted as a function of time at two points in the wake of a cylinder for $Re = 100$. All lengths are nondimensionalized with respect to the diameter of the cylinder and the origin is located at the center of the cylinder. It has been noted in [40] that lift experienced by the cylinder varies with time that is similar to the vorticity variation shown for the point $P1$, ($x = 0.5044, y = 0.0$) in Fig. 1. The point $P1$ is at the wake center-line and it has zero time-averaged vorticity value, while the time variation of vorticity for the off-center point $Q1$, ($x = 8.0, y = 8.0$) indicates a shift from the initial value, till it settles down to a different mean. This shift in vorticity values is interesting in the context of the work reported in [24,40]. In the former, the authors introduced a new *shift mode* to account for such behaviour to develop a reduced order POD model, while in the latter, such a shift was noted naturally in the POD modes for flow past a cylinder for $Re = 60$.

Flow inside a LDC is a canonical example of internal flows that displays linear temporal instability and Hopf-bifurcation in the parameter space. Starting from a quiescent initial condition inside the cavity, flow evolves with continual creation of vorticity at the wall segments. During this early stage, the flow is highly transient. Thereafter, small scale disturbances are created near the top right corner of the cavity, as the lid moves from left to right and distinct vortices are formed due to linear temporal instability. Subsequently, the flow saturates due to nonlinearity to a multi-periodic state. In Fig. 2a, an instantaneous snapshot of the flow is shown for $Re = 8500$ at $t = 550$, with three points marked in the frame. In frames 2(b)–2(d), vorticity time-series are shown for these points, which have structural similarities with the variations shown in Fig. 1. However, the LDC flow starts from a strongly transient state to a multi-periodic equilibrium state about a nonzero mean. This is in contrast to flow past a cylinder where the lift experienced starts from zero to a time-periodic state with zero mean. Subtle aspects of computing the LDC flow by accurate methods are given in [37,38] which also discuss the topology and dynamics of various vortical structures. The top lid, as driven from left to right, sets in an orbital motion of two sets of gyrating vortices around the weak triangular vortex at the center – as seen in Fig. 2a. Additionally, there are three corner vortices which display initial temporal instability followed by nonlinear saturation. In contrast, at the core of the cavity, vorticity values are orders of magnitude lower. The point P ($x = 0.95, y = 0.95$) also displays a nonzero mean vorticity whose time variation about this mean is symmetric, similar to time variation of vorticity on the center line of the cylinder-wake (with zero mean). Vorticity variations for the points at Q ($x = 0.95, y = 0.05$) and R ($x = 0.07, y = 0.17$) are different, with strong monotonic variation for the former. For both these points, time-periodic variation is not symmetric about the mean.

For both the flows after the transients have disappeared, the vorticity perturbation can be expressed by Galerkin-type expansion in terms of various instability modes present [9,42,44],

$$\omega'(\vec{X}, t) = \sum_{j=1}^{\infty} \left[A_j(t) f_j(\vec{X}) + A_j^*(t) f_j^*(\vec{X}) \right] \quad (6)$$

where A_j represents time-dependent amplitude function of the disturbance field, while f_j 's belong to a complete set of space-dependent functions satisfying boundary conditions. In Eq. (6), quantities with asterisks denote complex conjugates. If the complex amplitude is given by, $A_j(t) = (const.)e^{s_j t}$, during the linear growth

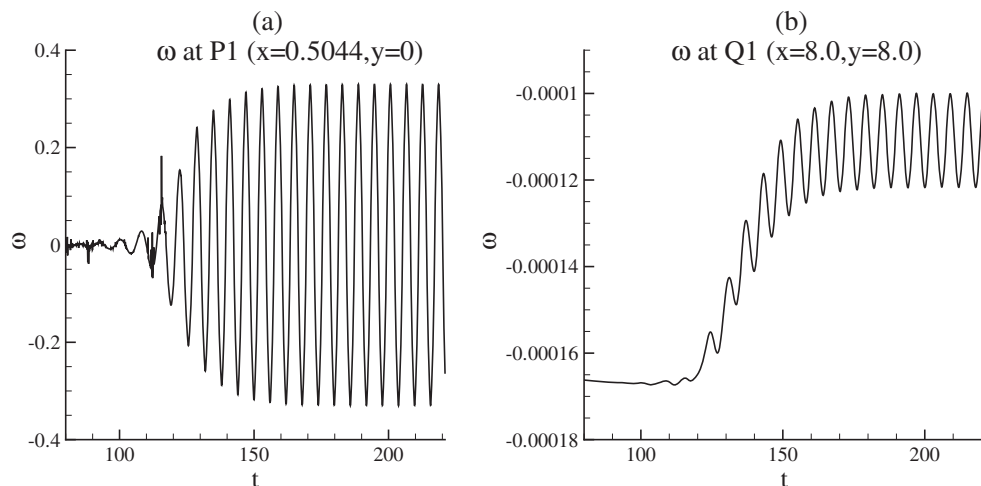


Fig. 1. Time variations of computed vorticity shown for flow past a circular cylinder for $Re = 100$ at (a) a point on the wake center line, $P1$ ($x = 0.5044, y = 0.0$) and (b) a point offset from the wake center line, $Q1$ ($x = 8.0, y = 8.0$). The center of the unit diameter cylinder is located at origin.

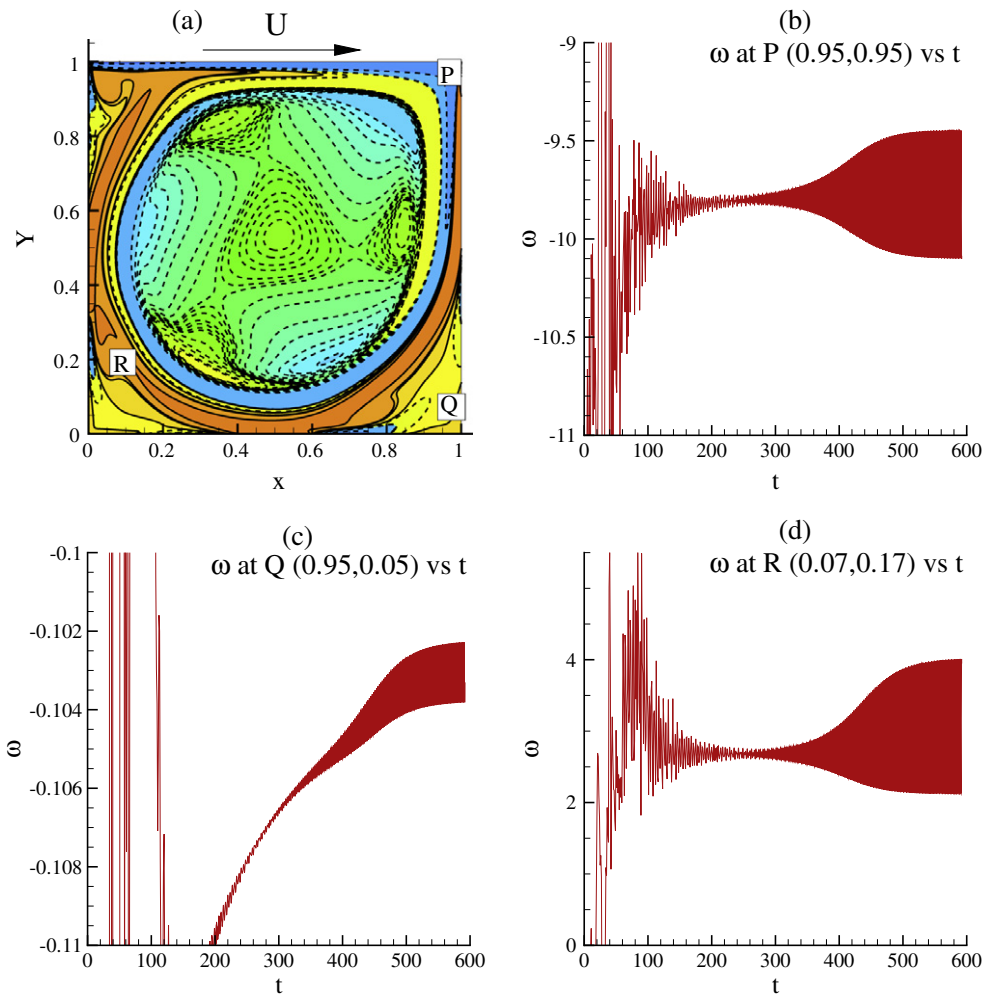


Fig. 2. (a) Computed vorticity flow field of flow inside a square lid-driven cavity for $Re = 8500$ shown at $t = 550.0$. (b–d) The time variations of vorticity at P, Q and R (as in frame (a)) are shown plotted, respectively.

stage, then the individual modes are governed by $\frac{dA_j}{dt} = s_j A_j$. Beyond this linear stage, disturbance field saturates due to nonlinearity expressed by the following LSE equation, obtained by eigenfunction expansion process in [9,10],

$$\frac{dA_j}{dt} = s_j A_j + N_j(A_k) \quad (7)$$

where $N_j(A_k)$ accounts for all nonlinear interactions among the modes (including self-interaction). This equation should not be confused with the celebrated Stuart–Landau equation [9,20]. Irrespective of the number of modes present many researchers, following Stuart–Landau equation, have considered only a single dominant mode with $s_j = \sigma_r + i\omega_1$ representing its linear complex temporal growth exponent. The proposed model in [20] was only for the amplitude of the leading mode, whereas authors in [9,44] derived it from the governing Navier–Stokes equation for both the amplitude and the phase. With a single mode in consideration, Landau and Stuart considered the self-interaction term only in (7) as $N_j = -\frac{l}{2} A |A|^2$, where $l = l_r + i l_i$ is the Landau coefficient. Writing $A = |A|e^{i\theta}$, one can rewrite (7) for the amplitude and phase of the leading mode (A) as,

$$\frac{d|A|^2}{dt} = 2\sigma_r |A|^2 - l_r |A|^4 \quad (8)$$

$$\frac{d\theta}{dt} = \omega_1 - \frac{l_i}{2} |A|^2 \quad (9)$$

In the literature, presence of other modes is assumed to produce negligible effects, as implied in the Stuart–Landau equation and an equilibrium amplitude (A_e) is obtained from (8) as, $|A_e| = \sqrt{2\sigma_r/l_r}$. However, time variations in Figs. 1 and 2 clearly show the presence of other significant modes, which cannot be neglected. To characterize nonlinear action on the linear temporal instability, we plot the time averaged computed equilibrium value (as defined in [40]) of disturbance vorticity for a range of Reynolds numbers for these two flows.

In POD, a space–time dependent field ω' is represented by eigenvectors, ϕ_i 's such that the projection of the latter to the former is maximized, i.e., the quantity $|\omega' \phi_i|^2$ is maximized subject to given initial and boundary conditions. Although POD technique was developed for stochastic dynamical system, its extension to study flow instabilities was advanced in [40]. Without going into details, one can show that the vectors ϕ_i come out as a solution of an integral eigenvalue relation given by,

$$\int_{\text{region}} R_{ij}(r, r') \phi_j(r') dr' = \lambda_i \phi_i$$

where the kernel of the integral is the two-point correlation function. For a system with finite energy content, Hilbert–Schmidt theory applies and there are countably infinite orthogonal eigenfunctions, ϕ_i .

It is natural to relate the obtained POD modes with the instability modes referred to above in Eqs. (6)–(9). One of the major contributions in [40] was to relate these. This was performed with the help of normalization factor given by $\epsilon_j = (\lambda_{2j-1} + \lambda_{2j}) / \sum_{l=1}^M \lambda_l$ via,

$$A_j(t) = \epsilon_j [a_{2j-1}(t) + i a_{2j}(t)] \quad (10)$$

$$f_j(\vec{X}) = \frac{1}{2\epsilon_j} \left[\phi_{2j-1}(\vec{X}) - i \phi_{2j}(\vec{X}) \right] \quad (11)$$

This normalization is appropriate as the eigenvalues of the covariance matrix determine the corresponding contribution of enstrophy of the flow field to the overall disturbance field. This is a new procedure to investigate flow instability as a spatio-temporal event for the flow in studying global nonlinear instability, provided one can obtain the POD modes as accurately as possible. In this context, Stuart–Landau equation or its generalization in LSE equations [40] provide a means of investigating flow instabilities.

We note that the time-series of disturbance vorticity also indicates the time variation of the instability amplitude $A_j(t)$. Thus, the saturated vorticity disturbance amplitude also indicates the equilibrium amplitude of the most dominant instability mode. In Fig. 3a, the equilibrium amplitude (A_e) of disturbance vorticity for the flow in LDC at the point P is shown plotted as a function of Re . If the flow was completely dominated by a single mode (that varied continuously with Re), then this variation would simply be parabolic. However, the discontinuous variation of A_e indicates multiple Hopf-bifurcations, as discussed in [40] for flow past a circular cylinder. In Fig. 3a, we have drawn three equivalent parabolic segments, meeting the Re axis at three critical values indicating three possible Hopf-bifurcations for the flow in LDC. Although the figure also indicates other possible bifurcations, the drawn sequences are meant to illustrate multiple bifurcations possible for the type of flows investigated in the present work. In [40] also, three definitive Hopf bifurcations were indicated for flow past a circular cylinder, based on computational and experimental evidences.

For flow past a cylinder, the onset of instability is characterized by the critical Reynolds number, Re_{cr} , which is reported differently by different investigators. The primary linear instability for flow past a cylinder examined computationally in [1,15,23,47] lies in the range, $45 \leq Re_{cr} \leq 47$, but the computational results presented in [39,40] using very high accuracy method obtained $Re_{cr} = 53.29$, thereby showing the dependence of Re_{cr} upon the numerical noise environment. This primary instability is synonymous to the first Hopf-bifurcation as defined in [12]. Looking at experimental evidences collected over decades, one notices a wide range of values for critical Reynolds number. Batchelor [2] conjectured $30 \leq Re_{cr} \leq 40$; Landau and Lifshitz [21] quoted it as 34; Kovasznay [19] reported $Re_{cr} = 40$, while Roshko [29] reported $Re_{cr} = 50$; Kiya et al. [17] obtained $Re_{cr} = 52$ and Tordella and Cancelli [46] reported this as 53. The sensitive dependence of the first Hopf-bifurcation or primary instability on facility-dependent disturbances becomes evident from experimental results of Homann [14], who showed $Re_{cr} \approx 65$. This result has been now satisfactorily explained in [40], by noting that the working medium used was a highly viscous oil, which effectively damped disturbances, thereby bypassing the first Hopf-bifurcation. Visualization pictures of [14] have been reproduced in [2,32] which show for $Re = 32$, the flow to be stable. For $Re = 55$, attached pair of bubbles remained, but the far-wake undulated and oscillated. This is not a result of Bénard–Kármán instability that causes alternate shedding of vortices in the wake. Observed phenomenon is due to Kelvin–Helmholtz instability of the pair of bubbles buffeted by convected weak disturbances in the free stream – as explained in [40]. However at $Re = 65$, the pair of wake bubbles loose top-down symmetry and vortices are shed alternately. This sequence of events and the computed results

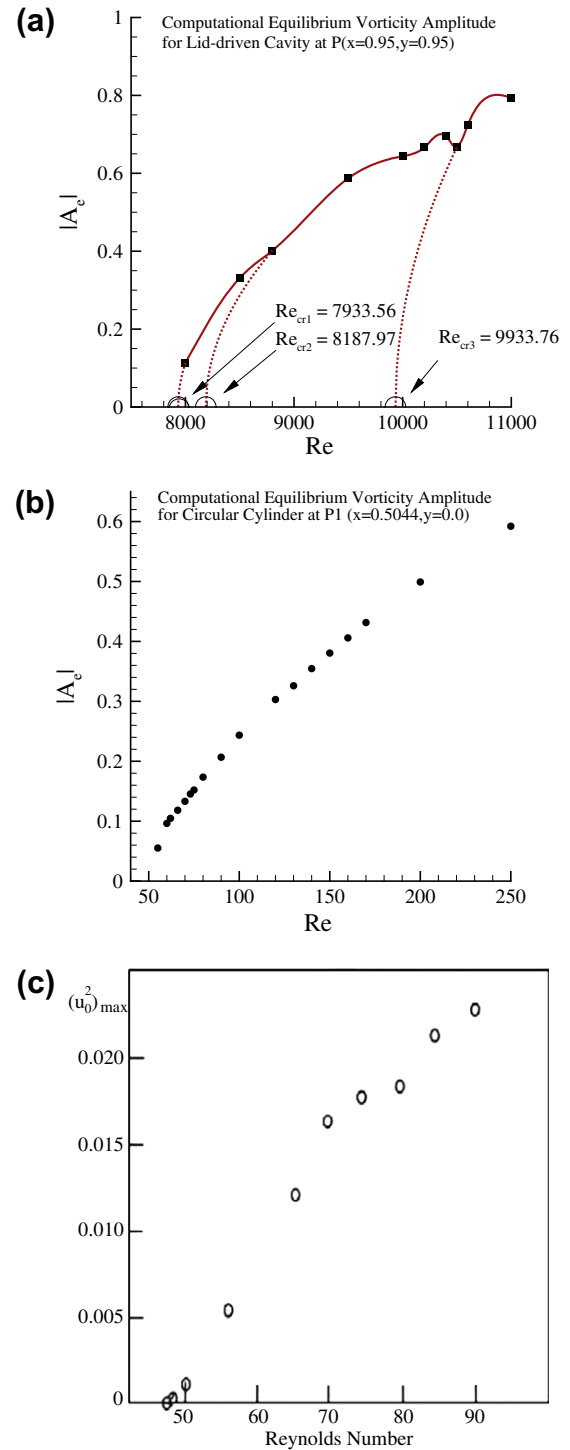


Fig. 3. (a) Equilibrium amplitude of the computed vorticity variation plotted against Re for the flow in LDC with critical Reynolds numbers for the point P ($x_P = 0.95, y_P = 0.95$). (b) Computed equilibrium amplitude of the disturbance vorticity variation plotted against Re for flow past a circular cylinder at a point $P1$ ($x_{P1} = 0.5044, y_{P1} = 0.0$). (c) Experimental data from [35] showing variation of amplitude of fluctuating velocity with Re for flow past a circular cylinder measured at 8D behind the cylinder on the wake center line.

shown in Fig. 3b, clearly shows the first Hopf-bifurcation is bypassed in [14]. However, an instability of lee-side bubbles causes periodically shed vortices for $Re = 65$, which is due to the second Hopf-bifurcation. Experimental results in [43] also suggest qualitative change in flow dynamics in the Reynolds number range between $Re = 60$ and 90 , as shown in Fig. 3c.

For flow past cylinder, multiple Hopf-bifurcations are also presented in Fig. 3b and c from the computed and experimental data from [40,43], respectively. Non-parabolic variation of A_e with Re in these figures indicates more than one bifurcation. Observed variation of A_e with Re is either due to presence of dominant multiple modes at different Reynolds numbers or their continuous presence at all Re , but with different mutual interactions for different ranges of Re . The behavior in experiments and computations can also be due to a combination of both of these effects simultaneously. In [40], it was interpreted that A_e versus Re curve begins with the first Hopf-bifurcation and there is a second bifurcation originating at a higher Reynolds numbers and these curves merge at the discontinuities, like that is noted in the experimental data in [43] near $Re = 80$ in Fig. 3c and the computational results from [40] reveal a similar discontinuity for Re above 75 in Fig. 3b.

These similarities seen for the flow in LDC and the flow past a cylinder seen in Fig. 3, indicate universal features of temporal instabilities of such flows. This is further investigated by other diagnostic tools to probe similarities and dissimilarities in the next section.

4. Proper orthogonal decomposition and spatio-temporal structures in flows

Here, we look at the spatio-temporal structures of multiple modes for the computed flows by POD analysis, as described in

[8,13,40,41]. However, we note the essential difference of performing POD in the presented approach here with that performed in [22,24,33] and references contained therein. In these latter references, POD analysis is based on spatial SVD analysis performed on solution of Navier–Stokes equation which is either obtained by RANS or unsteady RANS (URANS) approach. In contrast, our approach is based on performing POD by method of snapshots on time accurate solution of unsteady Navier–Stokes equation without resorting to any modeling, whatsoever.

Here, a number of flow field snapshots (M) are taken from the computed data, to use the method of snapshots developed in [41]. Note that all the simulations reported are for unsteady flows and the presented analysis follows identical procedure adopted in [40]. Disturbance vorticity field is calculated in the following fashion: over a chosen time interval, time-average of vorticity is calculated at every point of the domain. Disturbance vorticity ω' is obtained as the difference between the instantaneous field and the calculated time-averaged value. If one defines disturbance vorticity field as,

$$\omega'(\vec{X}, t) = \sum_{m=1}^M a_m(t) \phi_m(\vec{X}),$$

then ϕ_m 's are the eigenvectors of the covariance matrix whose elements are defined as,

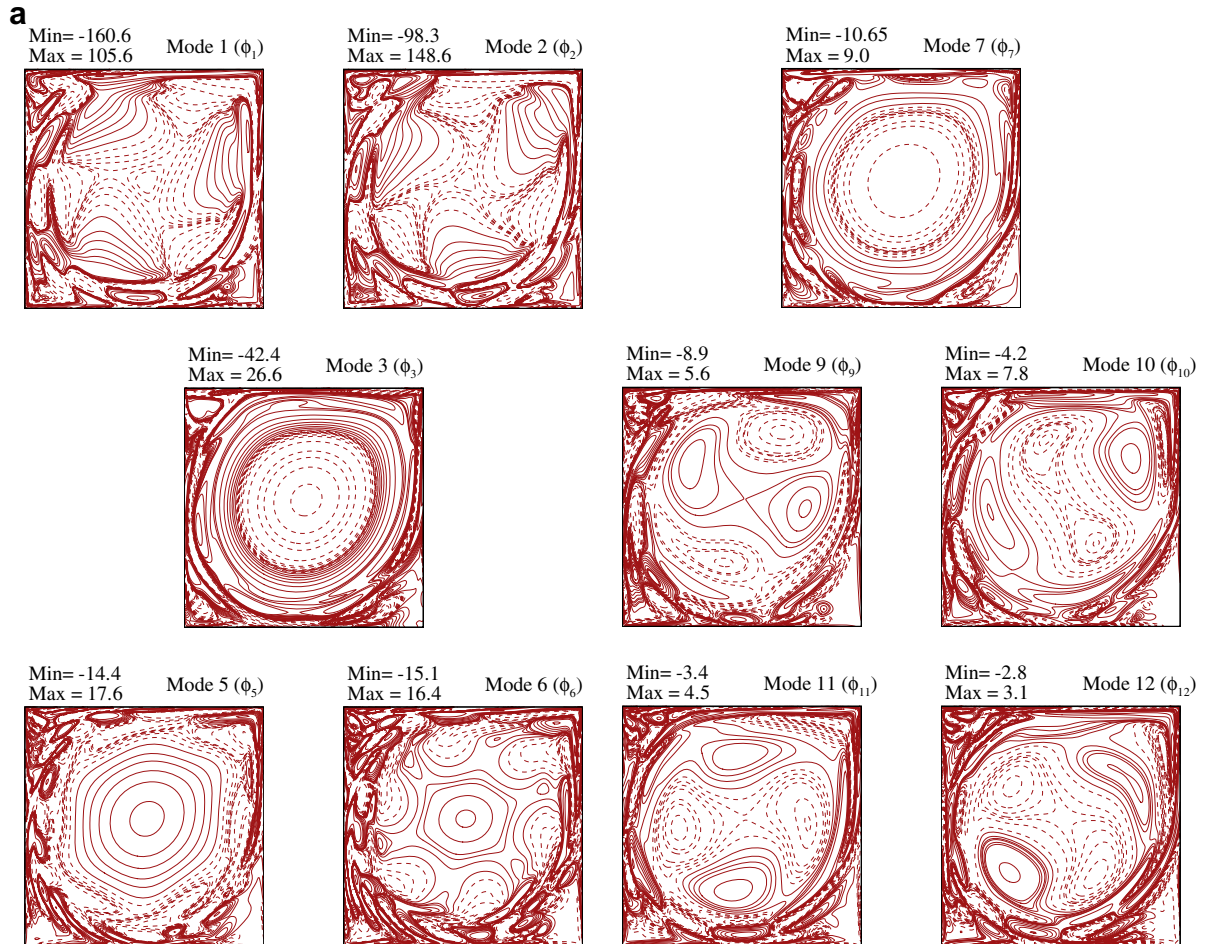


Fig. 4. (a) First six eigenfunctions for the LDC flow for $Re = 8500$ shown from the data set $t = 201$ –592. First two modes form pair, as also the fifth and sixth modes. The third mode is an isolated mode without forming any pair called as T_1 -mode. Maximum and minimum values are indicated which are of same order for the paired modes. (a) Higher eigenfunctions for the LDC flow for $Re = 8500$ shown for the data set from $t = 201$ –592. The seventh mode is an isolated mode without forming any pair while the 9th–10th and 11th–12th modes form pairs. Maximum and minimum values are of same order for the paired modes. (b) Time-dependent POD amplitude functions for the LDC flow for $Re = 8500$ during $t = 201$ –592. The modes $(a_1 - a_2)$; $(a_5 - a_6)$; $(a_9 - a_{10})$ and $(a_{11} - a_{12})$ form pairs, with a_3 and a_7 as the T_1 -modes. Modes a_9 to a_{12} are anomalous type T_2 -modes, those do not follow the time variation given by Stuart–Landau and LSE equations as discussed in the text.

$$R_{ij} = \frac{1}{M} \sum \omega'(\vec{X}_i, t_m) \omega'(\vec{X}_j, t_m),$$

with $ij = 1, 2, \dots, N$ defined over all the collocation points in the domain. Corresponding eigenvalues give the probability of occurrence of various modes for the disturbance field. Their partial sums give the cumulative enstrophy of the system,

$$En = \sum_{i=1}^N \omega^2(\vec{X}_i, t_m)$$

One of the interesting features of POD analysis is the dominant role played by various modes during different time intervals of flow instabilities, as explained for the flow past a circular cylinder in [40]. Numbering of POD modes signifies the contribution to enstrophy of a mode, with lower numbered ones contributing larger values. Definitions of different types of POD modes are possible for general fluid flow. We have already noted the connection between POD modes with instability modes defined in Eq. (10). Modes whose amplitude variation can be adequately expressed by the classical Stuart–Landau equation are termed as the regular or R-modes. There are two additional types of modes classified in

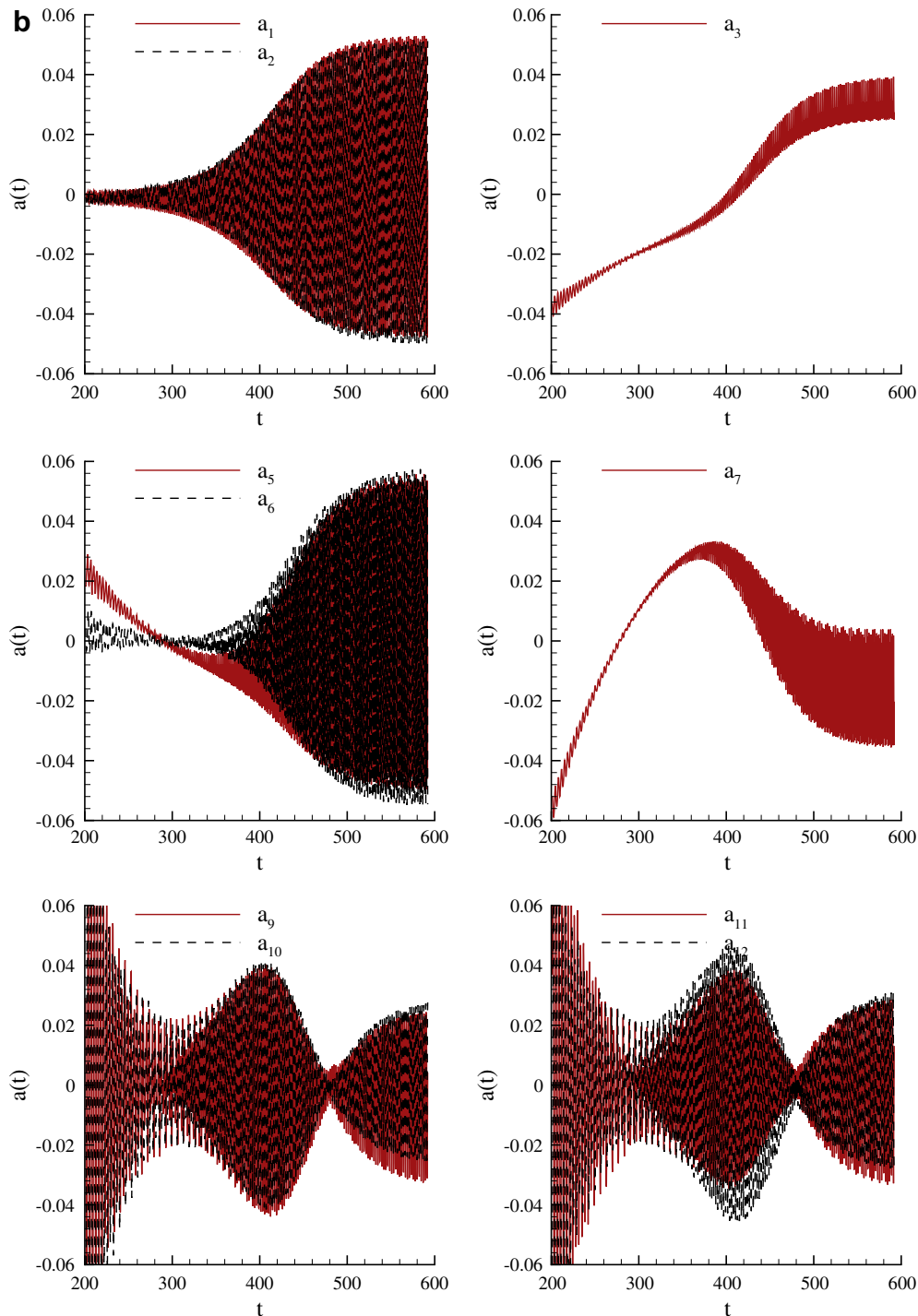


Fig. 4 (continued)

[40] as anomalous ones which do not satisfy the classical Stuart–Landau equation. One such POD modes' amplitude shows primarily, a non-periodic shift with time and hence, called the shift mode in [24]. While theoretically it is possible to obtain multiplicity of shift modes (as claimed in [24,33]), however, only the first shift mode is reported in these references to account for mean field only. However, following the procedure of [40], the leading modes contributing to the disturbance enstrophy are obtained here that can have more than one shift mode among these.

Additionally in [40], another type of instability modes are presented which do not satisfy Stuart–Landau equation while the associated POD modes show wave-packet like time variation. Thus, these modes are not present continually and can decide upon the ensuing flow instabilities and bifurcations. We revisit this classification in this work for the LDC flow problem, and existence of these testify the universal presence of these anomalous modes in both internal and external flows.

We first investigate the flow inside the driven cavity for $Re = 8500$, this Re is in between the second and the third Hopf-bifurcations shown in Fig. 3a. Time interval considered for POD spans from $t = 201$ to 592 and the covariance matrix is formed using M snapshots from $t = 201$ to 592 with an interval of 0.2. In Fig. 4a, we have shown first ten eigenfunctions, following the same numbering sequence of the POD modes explained in [40] and repeated briefly here using the eigen spectrum for the flow in LDC. For this flow, the first few eigenvalues are obtained as $\{\lambda_1 = 0.02917; \lambda_2 = 0.02435; \lambda_3 = 0.00301; \lambda_5 = 0.00059; \lambda_6 = 0.00049; \lambda_7 = 3.651 \times 10^{-4}; \lambda_9 = 9.82 \times 10^{-5}; \lambda_{10} = 7.51 \times 10^{-5}; \lambda_{11} = 3.52 \times 10^{-5}; \lambda_{12} = 2.83 \times 10^{-5}\}$. Numbering of these eigenvalues and the reason for the missing ones, will become apparent by looking

at the corresponding eigenfunctions shown in Fig. 4a. These eigenfunctions indicate that the first and the second mode form a regular pair (as described in [8,24,40]) and this is the R -mode.

Having obtained the snapshots and the eigenfunctions in the chosen time range, one can calculate the POD amplitude functions from Eq. (12) as,

$$a_i = \frac{\int \int_S \omega' \phi_i dS}{\int \int_S \phi_i^2 dS},$$

by using the orthogonal property of the eigenfunctions. It should be noted that to obtain the POD amplitudes correctly, one needs to take the number of snapshots which have been taken for the results presented here and in [40]. Without these many number of snapshots, amplitude functions would be obtained inaccurately. For the flow in LDC, these amplitudes are shown in Fig. 4b. Pairing of modes is taken into account in plotting the consecutive amplitudes either together or separately. Such identification becomes even more clearer upon viewing the POD amplitude functions depicted in Fig. 4b.

Third and seventh POD modes are isolated without forming pair and these are termed here as the anomalous T_1 -modes. These modes are similar to those identified as the *shift mode* in [24] for flow past circular cylinder. We note that the shift mode was modeled in [24], while it appeared directly from the time-accurate simulation in [40]. These modes were absent during $350 \leq t \leq 430$ for $Re = 60$, implying T_1 -modes are attributes of transient. These T_1 -modes for LDC are characterized by circular vorticity contours in the center of the cavity shown in Fig. 4a, along with the corner vortices. Isolated ϕ_3 -mode implies absence of the fourth mode.

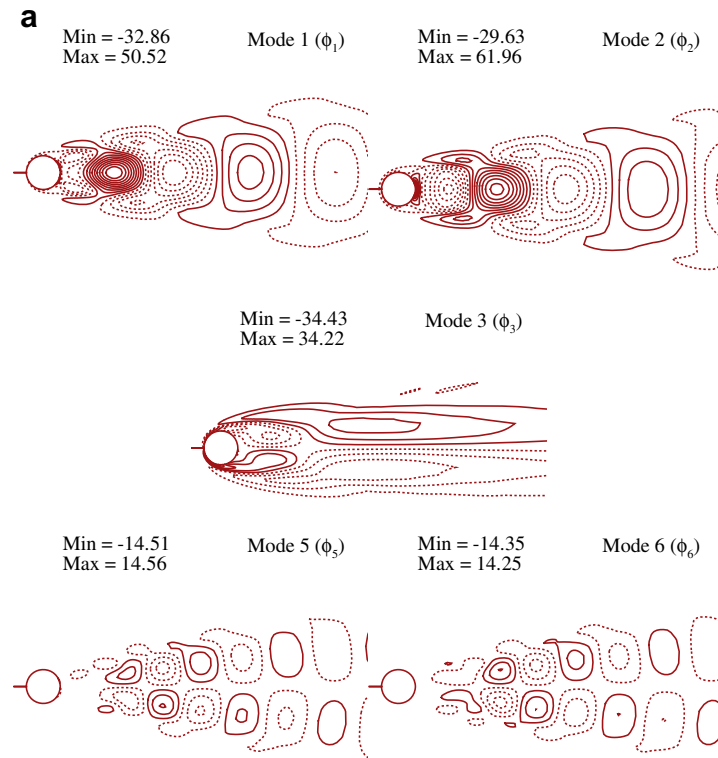


Fig. 5. (a) First six leading eigenfunctions for the flow past a circular cylinder for $Re = 100$ shown for the data set from $t = 80$ –221. First two modes form pair as also the fifth and sixth modes. The third mode is a T_1 -mode. Maximum and minimum values are of same order for the paired modes. (b) Time-dependent POD amplitudes for flow past a circular cylinder for $Re = 100$ during $t = 200$ –350. The modes $(a_1 - a_2)$; $(a_5 - a_6)$; $(a_7 - a_8)$ and $(a_9 - a_{10})$ form pairs, with a_3 and a_{11} are T_1 -modes. Modes a_5 – a_{10} are anomalous T_2 -modes, those do not strictly follow the time variation given by Stuart–Landau and LSE equations as discussed in the text.

The first-second and the fifth-sixth modes show time variations similar to that given in Fig. 2b and they are labeled as R -modes. It is noted that ϕ_5 and ϕ_6 have distinct hexagonal core vortical structures. The modes (ϕ_9, ϕ_{10}) and (ϕ_{11}, ϕ_{12}) again form pairs, but their time variations are different from R -modes. In [40], these wave-packet like variations have been identified as the second type of anomalous modes (T_2 -modes), as they cannot be represented as solution of (8). No model of instability exists that displays this type of time variation. Depicted 12 eigen modes (including the blank ones) account for 99.93% of the total enstrophy during the time interval $200 \leq t \leq 592$.

In Fig. 5a, eigenfunctions for flow past a cylinder are shown for $Re = 100$. In [40], results have been presented for $Re = 60$. The choice of Reynolds number for the presented case here matches the flow investigated in [24] for the same Re , but the formulation and numerical approaches are different. Thus, the present computed results and POD modes can be contrasted directly with those given in [24]. Also, presented results here are for the disturbance vorticity field, while disturbance velocity field is considered in [24]. Thus, the eigenvalues here are for enstrophy, while in [24], these are for kinetic energy. Here, the leading eigenvalues are given by, $\lambda_1 = 4.5963$; $\lambda_2 = 4.3843$; $\lambda_3 = 1.7291$; $\lambda_5 = 0.4934$; $\lambda_6 = 0.4908$;

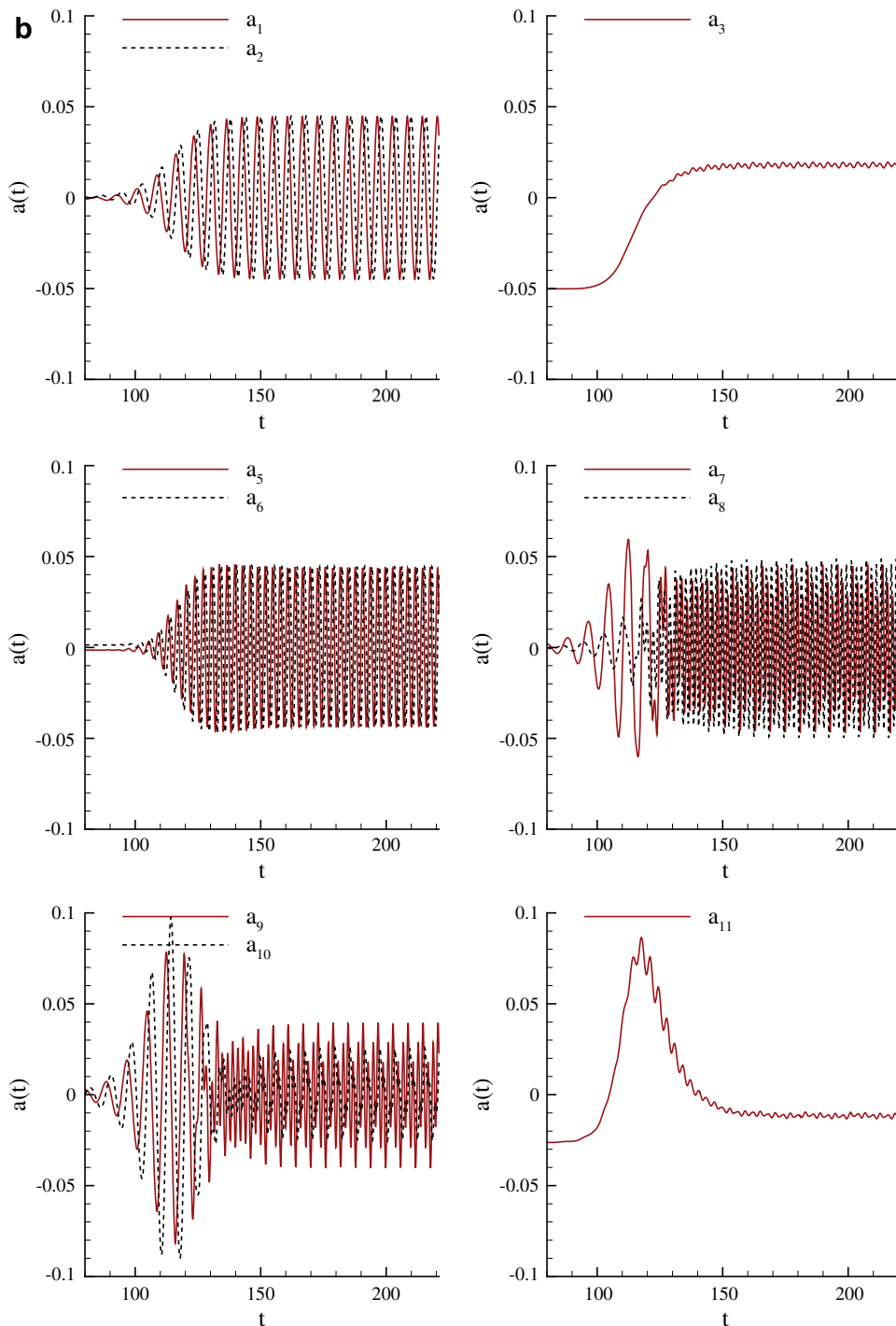


Fig. 5 (continued)

$\lambda_7 = 0.2107$; $\lambda_8 = 0.2092$; $\lambda_9 = 0.2071$; $\lambda_{10} = 0.1960$; $\lambda_{11} = 0.1327$; $\lambda_{13} = 0.0503$; $\lambda_{14} = 0.0426$ and these account for 97.95% of the total enstrophy. Altogether 19 POD modes are required to represent 99% of total enstrophy. This readily shows that with increasing Rey-

nolds numbers, more modes are required to reconstruct the dynamical system. Some of the POD amplitudes are shown in Fig. 5b. In this case, the third and the 11th modes are the T_1 – or the shift mode, as seen in Fig. 5b. However, unlike in [24], these

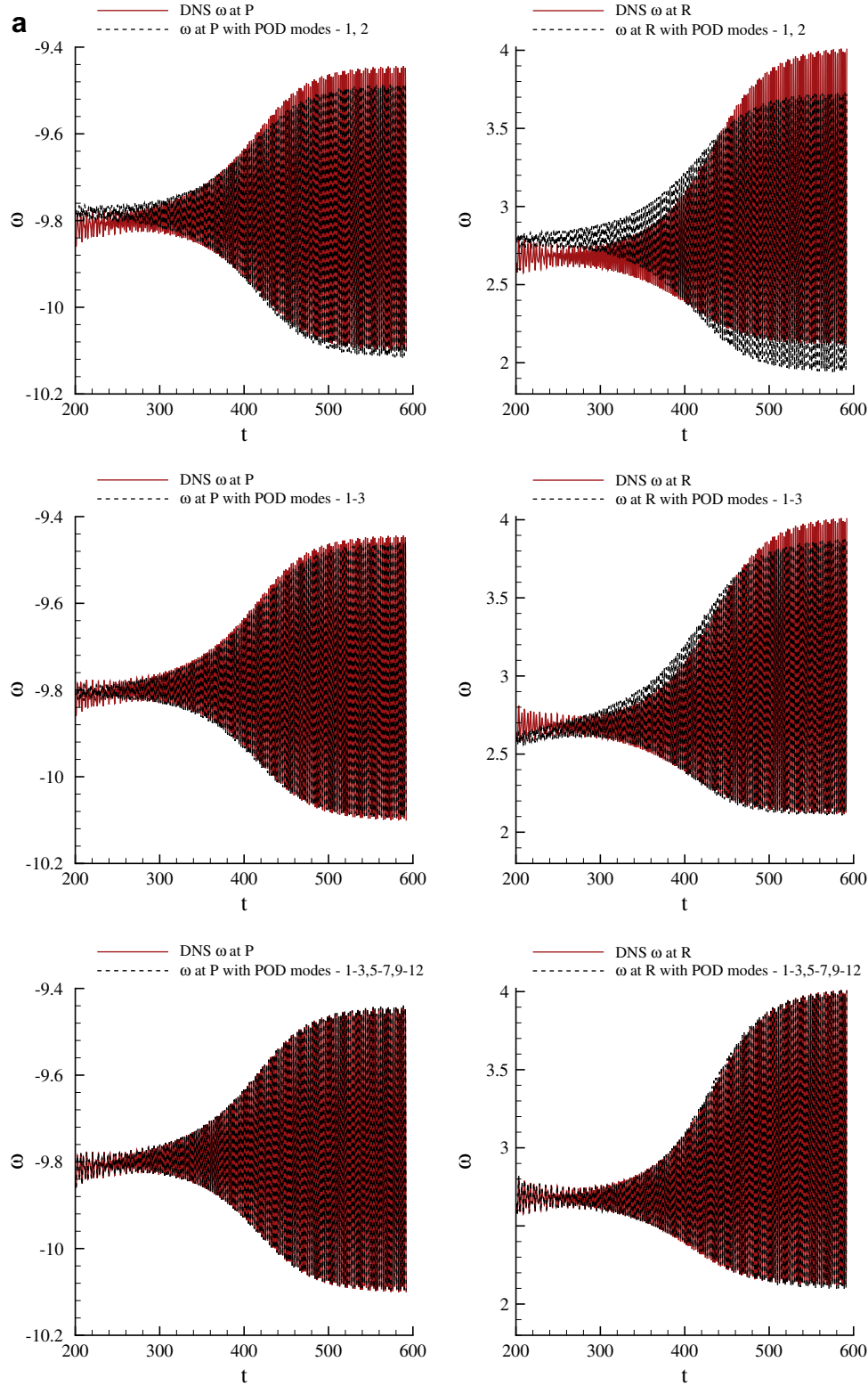


Fig. 6. (a) Comparison of reconstructed POD data with DNS results for LDC flow for $Re = 8500$ at two points P (left) and R (right). Note the proper shift caused by the inclusion of the third mode for both the points and the excellent match produced when 12 modes are included. (b) Comparison of reconstructed POD data with DNS results for flow past a circular cylinder for $Re = 100$ at two points $P1$ (left) and $Q1$ (right). Note the shift caused in the correct direction by including the third mode for point $Q1$. Very good match is produced when 19 modes are included.

modes appear directly from POD analysis of dense direct simulation data. For the pair consisting of fifth and sixth modes in Fig. 5b, amplitudes show a slight overshoot during the late growth stage, but this can still be termed as a R -mode. However, seventh–eighth and 9th–10th mode pairs' time variation is not given by Stuart–Landau or LSE equations [40] during the growth phase shown

in Fig. 5b. For the seventh–eighth modes pair, amplitude of a_7 displays wave-packet like time variation in the growth phase, while a_8 does not show such behaviour. Thus, the instability mode depicted by seventh and eighth modes depict an interaction between R - and T_2 -mode. In contrast, ninth and tenth modes display wave-packet like behaviour at early times for both the members of the pair. This

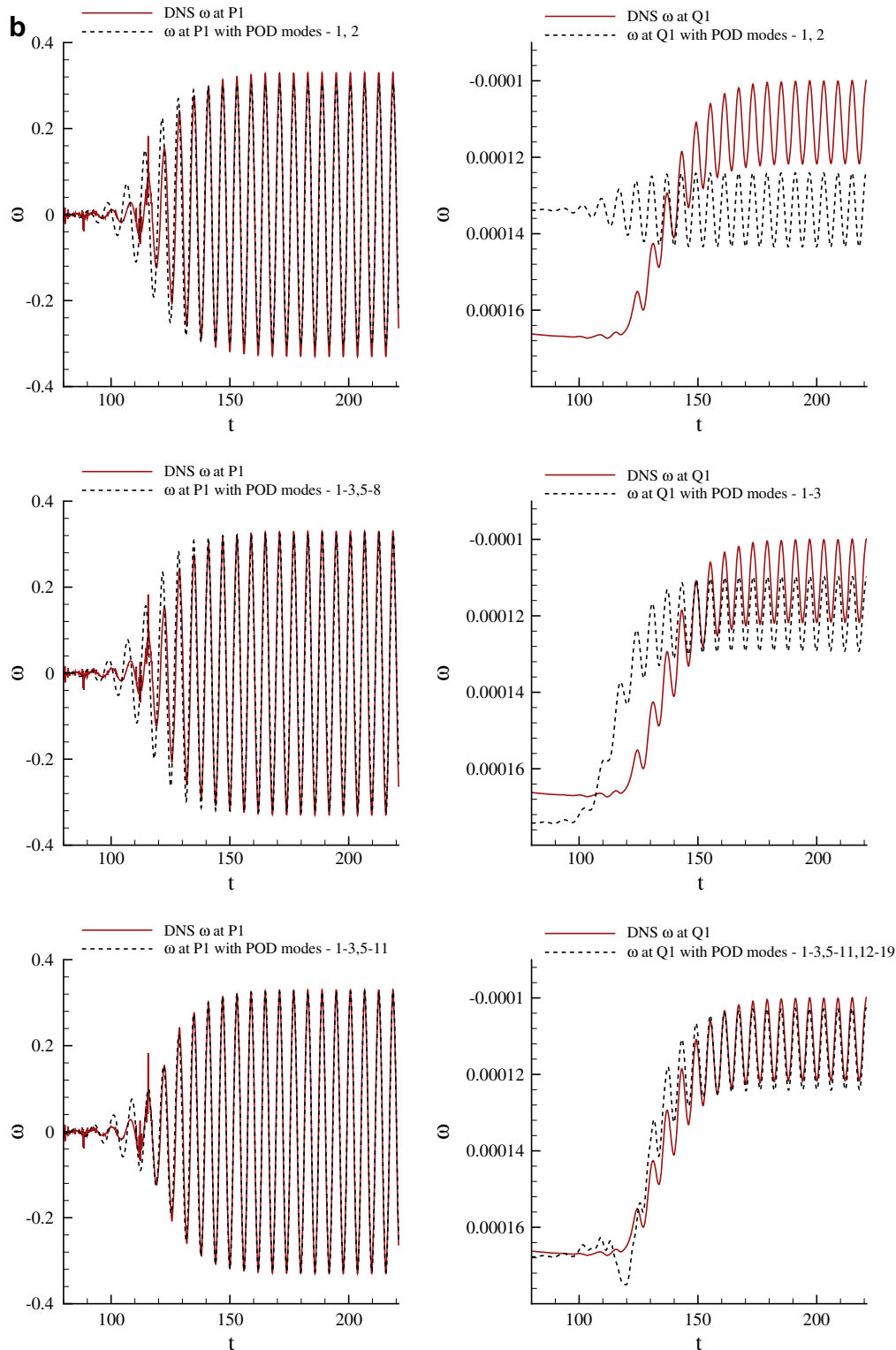


Fig. 6 (continued)

is similar to the behaviour noted in Fig. 10 of [40] for $Re = 60$ for the 13th–14th mode pair, where both the members of T_2 -modes displayed wave packet-like variations at early times.

5. Reconstruction of POD modes

To show that the obtained POD modes have adequate accuracy, in Fig. 6a and b, we show reconstructed signals for the flow in LDC and the flow over the cylinder, respectively. Apart from validating the POD procedure, this also brings into focus the roles of specific modes, in particular the roles of the anomalous modes. In Fig. 6a, reconstructed vorticity values at the points P and R are compared with the computed data for the flow in LDC. For the point P , when only the leading pair is used, there is mismatch at early times, as well as during the equilibrium stage. It is interesting to note that the addition of the anomalous third-mode improves the match with DNS data significantly at early times, without which we noted large shift before. Thus, the third mode plays the role of providing the correct shift to the solution. The match improved further when the fifth–seventh and 9th–12th modes are added. In the same way, for the point R , the instability is associated with asymmetric growth, the leading pair shows significant difference between the DNS data and the reconstruction. Just with the addition of the first anomalous mode, one notices significant improvement in the match. This match improves significantly when additional modes are included, as shown in the bottom right frame of Fig. 6a.

In Fig. 6b, reconstructed POD modes for vorticity are compared with the computed results for the flow past a cylinder for $Re = 100$ at the two indicated points. Results for the point $P1$ on the wake centerline in the left column, show that one needs to include first 11 modes to reconstruct the signal during the growth and the non-linear saturation stage. However, this still does not provide good match with the solution at early transient stages, for which we have noted that we require at least 19 modes to account for 99% of the total enstrophy. On the right column of Fig. 6b, results of reconstruction of POD modes for the point $Q1$ are compared with the computed solutions. Here, the leading modes show very poor reconstruction and once again exposes the inadequacy of attempts

to explain the flow instability by the sole leading instability modes, as is usually done using Stuart–Landau equation. Inclusion of the first anomalous mode (third mode), improves the match significantly. Although the match improves even further when 19 modes are included (as shown in bottom right frame), there is residual mismatch during early transient and growth stages. We close this section by noting that it is not adequate to check the effectiveness of POD by reconstructing the solution for the cylinder only along centerline. This reconstruction scheme can be judged by doing the same globally in the domain.

6. Modeling anomalous modes

We have already established a relationship between the POD and the instability modes in Eqs. (10) and (11). The leading instability modes are in turn noted to be governed by Stuart–Landau equation [9,20,44] or LSE equations [40]. It was specifically noted in the last section that not all of the instability modes can be represented by either of these equations and the corresponding POD modes have been identified as anomalous modes.

In the following, we attempt to obtain empirical fits for both T_1 - and T_2 -types of anomalous modes. In Fig. 7a, the POD amplitudes are shown for the flow past a circular cylinder for $Re = 60$ during the time interval $200 \leq t \leq 350$ to highlight the anomalous modes. In Fig. 10 of [40], similar results were shown for the time interval $0 \leq t \leq 430$ and four T_1 -modes were detected before the appearance of first T_2 -modes. In Fig. 7a, a_3 is a T_1 -mode and (a_7, a_8) represent T_2 -mode. Despite the fact that the POD amplitudes appear to be in different order between the present Fig. 7a with Fig. 10 of [40], one can clearly see the connection and continuity between the respective modes in these two figures. For example, (a_1, a_2) , (a_5, a_6) follow each other closely, and so does a_3 in these two figures. Additional T_1 modes in Fig. 10 of [40] before the T_2 mode are actually of smaller values close to zero and moreover outside the time range considered in Fig. 7a. Thus, the description of modes in POD analysis are consistent, when one compares the modes in any time interval to highlight the presence or absence of mode

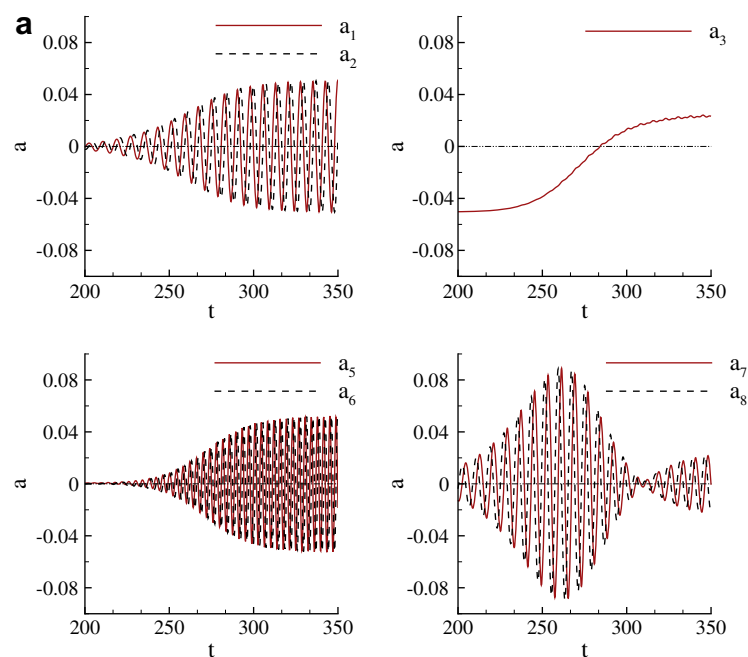


Fig. 7. (a) POD amplitude functions for the flow past a cylinder for $Re = 60$ during $200 \leq t \leq 350$. (b) POD amplitude functions for the flow in a LDC for $Re = 8500$ during $200 \leq t \leq 500$.

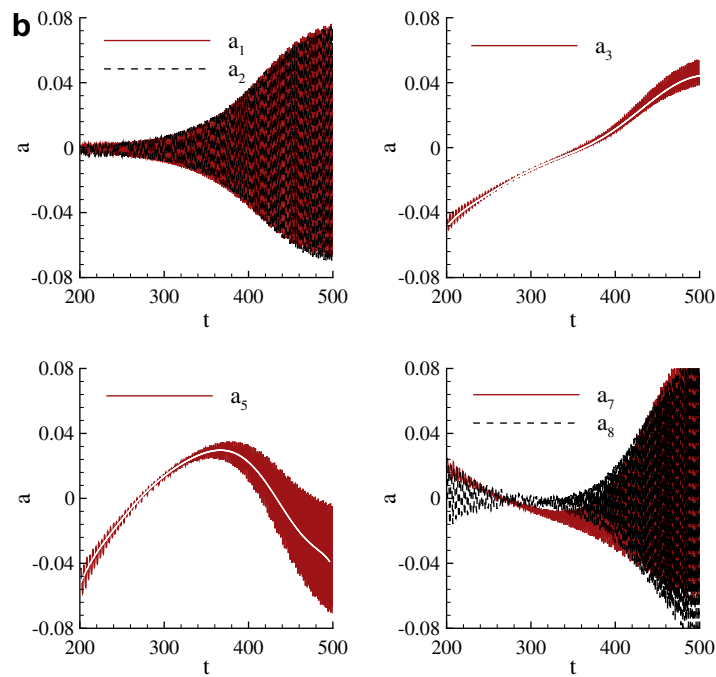


Fig. 7 (continued)

types – as has been done here in investigating a particular time interval to show the presence of T_1 – and T_2 -modes. The T_2 -anomalous mode formed by (a_7, a_8) can be expressed empirically by,

$$A_4 = A_{40} e^{-\alpha_4 |t-t_0|^2 - \beta_4 |t-t_0|^3 + i(\pi/2 - \omega_4 t)} \quad (12)$$

where $A_{40} = 0.0896343$; $t_0 = 313.80$; $\alpha_4 = 0.001617155$; $\beta_4 = -1.85866 \times 10^{-5}$ and $\omega_4 = 0.7888$.

In Fig. 7b, we have shown the POD amplitudes for the flow in LDC for $Re = 8500$ during the time interval, $200 \leq t \leq 500$. Purpose for doing so is to emphasize the role of transients in determining ensuing instability. We note that (a_5, a_6) and a_7 of Fig. 4b exchange numbering of the modes with that shown in Fig. 7b. This is essentially due to different quantum of enstrophy due to different time intervals. This also shows that taking longer time interval reduces the amplitude of the T_1 -mode (a_7 in Fig. 4b). In Fig. 7b, mean variation for the first two T_1 -modes, the third and fifth mode, can be expressed in terms of an eighth order polynomials: $\bar{A}_j(t) = \sum_{k=0}^8 p_{kj} t^k$, those can be expressed in terms of the following coefficients for \bar{A}_3 given by, $p_{03} = -15.52397$; $p_{13} = 0.362503$; $p_{23} = -0.0036543$; $p_{33} = 0.002065$; $p_{43} = -7.142 \times 10^{-8}$; $p_{53} = 1.5467 \times 10^{-10}$; $p_{63} = -2.048 \times 10^{-13}$; $p_{73} = 1.5184 \times 10^{-16}$; $p_{83} = -4.828 \times 10^{-20}$ and for \bar{A}_5 given by, $p_{05} = -62.4552$; $p_{15} = 1.596186$; $p_{25} = -0.017689$; $p_{35} = 1.10776 \times 10^{-4}$; $p_{45} = -4.283 \times 10^{-7}$; $p_{55} = 1.046 \times 10^{-9}$; $p_{65} = -1.577 \times 10^{-12}$; $p_{75} = 1.34014 \times 10^{-15}$; $p_{85} = -4.915 \times 10^{-19}$. These data fit for \bar{A}_3 and \bar{A}_5 are indicated by white lines in the second and the third frames of Fig. 7b. High frequency fluctuations about this mean do not follow LSE-type equations. Even when piece-wise cubic B-splines were fitted, one required more than 1000 nodes during $300 \leq t \leq 500$ only.

7. Conclusion

We have shown here that the new anomalous modes reported for flow past a circular cylinder in [40], are also present in the internal lid-driven cavity (LDC) flow. This has also been identified here with the help of POD analysis in a straightforward manner on results obtained by solving Navier–Stokes equation in real-time

with extremely accurate methods. While in other efforts, anomalous modes of the first kind have been explicitly modeled [22,24,33], here these are obtained directly from POD of simulation data. Identification of anomalous modes directly from POD for flow in LDC is performed for the first time. Novelty of this effort also lies in showing universal nature of the anomalous mode of first kind for both internal and external flows, which can be more than one in numbers.

The anomalous modes (T_1 - and T_2 -modes) also play central role during flow instabilities. This aspect has been studied here following the work reported in [40] by relating POD modes with instability modes. Once the instability modes are obtained, this opens up the possibility of performing nonlinear instability studies without any approximation. As the identified anomalous modes do not follow either the LSE [40] or the classical Stuart–Landau equations [9,20,44], we have proposed empirical data fits for these anomalous modes. It is noted that these anomalous modes can affect flow instabilities, not only for the internal and external flows studied here, but also for other flows as well.

References

- [1] Barkley D. Linear analysis of the cylinder wake mean flow. *Europhys Lett* 2006;75(5):750–6.
- [2] Batchelor GK. Introduction to fluid dynamics. UK: Cambridge Univ. Press; 1988.
- [3] Beckers M, van Heijst GJF. The observation of a triangular vortex in a rotating fluid. *Fluid Dyn Res* 1998;22:265–79.
- [4] Bruneau C-H, Saad M. The 2D lid-driven cavity problem revisited. *Comput Fluids* 2006;35:326–48.
- [5] Carnevale GF, Kloosterziel RC. Emergence and evolution of triangular vortices. *J Fluid Mech* 1994;259:305–31.
- [6] Cazemier W, Verstappen RWCP, Veldman AEP. Proper orthogonal decomposition and low dimensional models for driven cavity flows. *Phys Fluids* 1998;10(7):1685–99.
- [7] Chomaz J-M. Global instabilities in spatially developing flows: non-normality and nonlinearity. *Ann Rev Fluid Mech* 2005;37:357–92.
- [8] Deane AE, Kevrekidis IG, Karniadakis G Em, Orszag SA. Low-dimensional models for complex geometry flows: application to grooved channels and circular cylinders. *Phys Fluids A* 1991;3:2337–54.
- [9] Drazin PG, Reid WH. Hydrodynamic stability theory. UK: Cambridge University Press; 1981.

- [10] Eckhaus W. Studies in non-linear stability theory. New York (USA): Springer-Verlag; 1965.
- [11] Fortin A, Jardak M, Gervais JJ, Pierre R. Localization of Hopf bifurcations in fluid flow problems. *Int J Numer Methods Fluids* 1997;24(11):1185–210.
- [12] Golubitsky M, Schaeffer DG. Singularities and groups in bifurcation theory. New York (USA): Springer-Verlag; 1984.
- [13] Holmes P, Lumley JL, Berkooz G. Turbulence, coherent structures, dynamical systems and symmetry. UK: Cambridge Univ. Press; 1996.
- [14] Homann F. Einfluss grosser zahigkeit bei stromung um zylinder. *Forsch auf dem Gebeite des Ingenieurwesens* 1936;7(1):1–10.
- [15] Jackson CP. A finite-element study of the onset of vortex shedding in flow past variously shaped bodies. *J Fluid Mech* 1987;182:23–45.
- [16] Jorgensen BH, Sorenson JN, Brons M. Low-dimensional modeling of a driven cavity flow with two free parameters. *Theoret Comput Fluid Mech* 2003;16(4):299–317.
- [17] Kiya M, Suzuki Y, Mikio A, Hagino M. A contribution to the free stream turbulence effect on the flow past a circular cylinder. *J Fluid Mech* 1982;115:151–64.
- [18] Kosambi DD. Statistics in function space. *J Indian Math Soc* 1943;7:76–88.
- [19] Kovaszny LSG. Hot-wire investigation of the wake behind cylinders at low Reynolds numbers. *Proc Roy Soc Lond A* 1949;198:174–90.
- [20] Landau LD. On the Problem of Turbulence. *CR Acad Sci USSR* 1944;44:311–5.
- [21] Landau LD, Lifshitz EM. Fluid mechanics, vol. 6. London (UK): Pergamon Press; 1959.
- [22] Luchtenburg DM, Guenther B, Noack BR, King R, Tadmor G. A generalized mean-field model and high frequency actuated flow around a high-lift configuration. *J Fluid Mech* 2009;623:283–316.
- [23] Morzynski M, Afanasiev K, Thiele F. Solution of the eigenvalue problems resulting from global nonparallel flow stability analysis. *Comput Meth Appl Mech Eng* 1999;169:161–76.
- [24] Noack BR, Afanasiev K, Morzynski M, Tadmor G, Thiele F. A hierarchy of low-dimensional models for the transient and post-transient cylinder wake. *J Fluid Mech* 2003;497:335–63.
- [25] Peng Y-F, Shiau Y-H, Hwang RR. Transition in a 2-D lid driven cavity flow. *Comput Fluids* 2003;32:337–52.
- [26] Poliashenko M, Aidun CK. A direct method for computation of simple bifurcations. *J Comput Phys* 1995;121(2):246–60.
- [27] Provansal M, Mathis C, Boyer L, Benárd-von Kármán instability: transient and forced regimes. *J Fluid Mech* 1987;182:1–22.
- [28] Rempfer D. On low-dimensional Galerkin models for fluid flow. *Theoret Comput Fluid Mech* 2000;14(2):75–88.
- [29] Roshko A. On the drag and shedding frequency of two-dimensional bluff bodies. *NACA TN* 1954;3169.
- [30] Sahin M, Owen RG. A novel fully-implicit finite volume method applied to the lid-driven cavity problem: Parts I and II. *Int J Numer Methods Fluids* 2003;42:57–88.
- [31] Sarpakaya T. Nonimpulsively started steady flow about a circular cylinder. *AIAA J* 1991;29:1283–9.
- [32] Schlichting H. Boundary layer theory. New York: McGraw Hill Book Co.; 1987.
- [33] Siegel SG, Seidel J, Fagley C, Luchtenburg DM, Cohen K, McLaughlin T. Low-dimensional modelling of a transient cylinder wake using double proper orthogonal decomposition. *J Fluid Mech* 2008;610:1–42.
- [34] Sengupta TK, Dey S. Proper orthogonal decomposition of direct numerical simulation data of bypass transition. *Comput Struct* 2004;82:2693–703.
- [35] Sengupta TK, Lim TT, Sajjan SV, Ganesh S, Soria J. Accelerated flow past a symmetric aerofoil: experiments and computations. *J Fluid Mech* 2007;591:255–88.
- [36] Sengupta TK, Venkatasubbaiah K, Pawar SS. Nonlinear instability of mixed convection flow over a horizontal cylinder. *Acta Mech* 2008;201(1–4):197–210.
- [37] Sengupta TK, Lakshmanan V, Vijay VVSN. A new combined stable and dispersion relation preserving compact scheme for non-periodic problems. *J Comput Phys* 2009;228(8):3048–71.
- [38] Sengupta TK, Vijay VVSN, Bhaumik S. Further improvement and analysis of CCD scheme: dissipation discretization and de-aliasing properties. *J Comput Phys* 2009;228(17):6150–68.
- [39] Sengupta TK, Suman VK, Singh Neelu. Solving Navier–Stokes equation for flow past cylinders using single-block structured and overset grids. *J Comput Phys* 2010;229:178–99.
- [40] Sengupta TK, Singh Neelu, Suman VK. Dynamical system approach to instability of flow past circular cylinder. *J Fluid Mech* 2010;656:82–115.
- [41] Sirovich L. Turbulence and dynamics of coherent structures, Part I–III. *Quart Appl Math* 1987;45.
- [42] Sreenivasan KR, Strykowski PJ, Olinger DJ. Hopf bifurcation, Landau equation and vortex shedding behind circular cylinders. *Forum Unsteady Flow Separ* 1987:1–13.
- [43] P.J. Strykowski, The Control of Absolutely and Convectively Unstable Shear Flows, Ph.D. Thesis, Yale University, 1986.
- [44] Stuart JT. On the non-linear mechanics of wave disturbances in stable and unstable parallel flows. Part 1. The basic behaviour in plane Poiseuille flow. *J Fluid Mech* 1960;9:353–70.
- [45] Telionis DP. Unsteady viscous flows. New York (USA): Springer-Verlag; 1981.
- [46] Tordella D, Cancelli C. First instabilities in the wake past a circular cylinder. Comparison of transient regimes with Landau's model. *Meccanica* 1991;26:75–83.
- [47] Zebib A. Stability of viscous flow past a circular cylinder. *J Eng Math* 1987;21:155–65.